Journal of Magnetic Resonance **152,** 276–287 (2001)
doi:10.1006/jmre.2001.2414, available online at http://www.idealibrary.com on IDEAL®

Electron-Zeeman Resolved Electron Paramagnetic Resonance Spectroscopy

Rüdiger-A. Eichel and Arthur Schweiger[1]

Physical Chemistry, ETH Zürich, CH-8093 Zurich, Switzerland

Received June 5, 2001; revised July 16, 2001; published online September 6, 2001

Electron-Zeeman (EZ) resolved electron paramagnetic resonance (EPR) spectroscopy is introduced. In this two-dimensional pulse EPR technique a sinusoidal external field $\Delta B_0(t)$ of variable amplitude is applied during the pulse sequence, resulting in a field-swept EPR spectrum that is spread into a second dimension, representing the *g* values of the paramagnetic species. The method can be used to improve the resolution of polycrystalline and single-crystal EPR spectra. For polycrystalline systems, simplified EPR spectra are obtained for fixed *g* values. For axial symmetry, these spectra allow direct access to coupling constants, also at orientations that differ from the principal axes orientations. Furthermore, overlapping resonances can be disentangled, extra-absorption peaks identified and unresolved hyperfine splittings observed. The sum projection onto the *g*-value axis corresponds in a *g*-value spectrum, which is free of hyperfine interactions. A detailed theoretical description of the EZ-EPR experiment is given. Several model calculations for systems with different symmetry of the magnetic interaction tensors are presented, and the versatility of EZ-EPR is demonstrated for different paramagnetic systems with *g* anisotropy. © 2001 Academic Press

1. INTRODUCTION

In recent years, a variety of continuous-wave (cw) and pulse electron paramagnetic resonance (EPR) techniques have been developed, in order to enhance the spectral resolution of EPR spectra or to disentangle overlapping spectral features (*1, 2*). The methods are based, for example, on the difference in relaxation times of paramagnetic species (*3–5*), the selective driving of forbidden transitions (*6*), the orientation dependence of anisotropic systems (*7, 8*), or the dependence of the nutation frequency on the transition probability of a particular transition (*9, 10*).

To unravel overlapping EPR spectra of paramagnetic species based on the differences in the *g* values, the common approach is to go to high magnetic fields, because the electron-Zeeman (EZ) interaction increases linearly with the field (*11, 12*). Electron-Zeeman resolved EPR (EZ-EPR) (*13–15*) offers an alternative approach, exploiting that the only EPR relevant B_0-field dependent term in the spin Hamiltonian is the EZ interaction. The field-swept EPR spectrum can then be spread into a *second* dimension, representing the *g* values. The nuclear-Zeeman (NZ) interaction leads in first order only to a shift of the energy levels, which is independent of the magnetic quantum number m_S of the electron spin. Nuclear-Zeeman frequencies do not therefore manifest in the allowed transitions of an EPR spectrum.

The first EZ-EPR experiments were based on a hole-burning scheme combined with a field jump of a fixed amplitude and a variable evolution time (*13*), an approach which has proven to be technically rather inconvenient. Despite of the multiplex advantage of Fourier spectroscopy in the hole-burning experiment, the signal amplitude in an echo-detected approach is expected to be considerably higher, since the frequency range excited by an echo sequence is usually much larger than the width of the hole created by a selective pulse. First promising results have been obtained with the echo approach by using a primary echo and replacing the field step by a sinusoidal field modulation of variable amplitude (*14*). If the amplitude of the field modulation is changed instead of the evolution time, the EZ-EPR spectra are free of relaxational decays.

In general, technical shortcomings that appear when magnetic field jumps are applied can be overcome by using a field modulation. These are the relatively long times required to switch on and off the field, limitations in the field homogeneity, and stability during and shortly after the magnetic field pulse, as well as the limited reproducibility of the shape of the field pulses.

A concept similar to EZ-EPR is used in nuclear-Zeeman resolved ESEEM (*16*), which is based on a three-pulse ESEEM scheme. In this experiment a field jump is applied during the free evolution of nuclear coherence, allowing the coherence to accumulate additional phase. In NZ-ESEEM the nuclear transition frequencies are therefore correlated with the nuclear Zeeman frequencies.

Apart from EPR, pulsed magnetic fields have been used, for example, in Zeeman-perturbed NQR (*17*), where the external field is switched on only during the evolution period of a quadrupolar spin–echo sequence. Problems associated with the T_2 decay are eliminated by replacing the increasing evolving time by an increasing magnetic field. The same technique is applied to Zeeman-incremented multiple quantum NMR experiments (*18*), where again the external field is varied instead of incrementing the free evolution period. Such experiments give

[1] To whom correspondence should be addressed. E-mail: schweiger@phys.chem.ethz.ch.

1090-7807/01 $35.00

rise to simplified spectra in the multiple quantum domain, which are free from T_2 decays. Also in Zeeman-switched optical free-induction decay (OFID) spectroscopy (*19*), the transition frequency is changed by a pulsed magnetic field. The resulting frequency shift produces a heterodyne signal due to the interference with the radiation from coherence that is prepared with a small-frequency cw laser.

In this work, we first outline the principle of EZ-EPR and give analytical expressions for the theoretical description of the EZ-EPR experiment. In the following section, numerical simulations of a number of model systems serve to illustrate different features of EZ-EPR spectra. The experimental section comprises both, a short description of the additional setup for EZ-EPR and a discussion of the limitations related to this new method. In the final section, experimental results are given to demonstrate the potential and versatility of EZ-EPR spectroscopy.

2. THEORETICAL DESCRIPTION OF THE EZ-EPR EXPERIMENT

We describe the principle of EZ-EPR by considering an isotropic spin system with electron spin $S = \frac{1}{2}$ and one nuclear spin I. The resonance frequencies are then given by

$$\omega_{\text{res}} = \frac{g\beta_e}{\hbar} B_0 + m_I a_{\text{iso}}, \qquad [1]$$

with the nuclear magnetic quantum number $m_I = -I, \ldots, I$ and the isotropic hyperfine splitting a_{iso}. The resonance frequency of two transitions of two different species k and l with g values g_k and g_l, hyperfine splittings a^k_{iso} and a^l_{iso}, and magnetic quantum numbers m^k_I and m^l_I are the same if

$$\Delta g = g_k - g_l = \frac{\hbar}{\beta_e\, B_0} \left(m^l_I a^l_{\text{iso}} - m^k_I a^k_{\text{iso}}\right). \qquad [2]$$

A change in the B_0 field by ΔB_0 changes the g-value specific resonance frequencies by $\Omega_k = (g_k \beta_e \Delta B_0)/\hbar$ and $\Omega_l = (g_l \beta_e \Delta B_0)/\hbar$. The separation

$$\Delta\Omega_{kl} = \Omega_k - \Omega_l = \frac{\Delta g\, \beta_e}{\hbar} \Delta B_0 \qquad [3]$$

of the two transitions along the electron Zeeman axis is thus proportional to the difference in the g values and to the field change ΔB_0. This is shown schematically in Fig. 1 for two $S = \frac{1}{2}$, $I = \frac{1}{2}$ spin systems with different g values and different hyperfine couplings. Two lines, one from each system, overlap in the conventional EPR spectrum but are separated in a 2D EZ-EPR experiment according to their g-value difference.

EZ-EPR experiments can be carried out either with a polarization transfer scheme or a scheme where phase of electron coherence is accumulated. In this work, we concentrate on an EZ-EPR approach which consists of a primary electron spin–

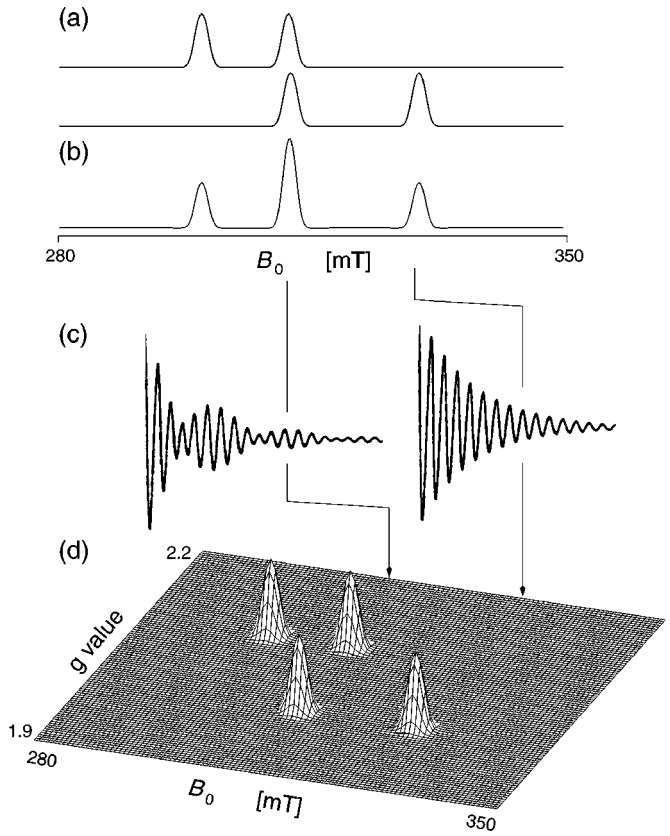

FIG. 1. Schematic illustration of electron Zeeman-resolved EPR for two paramagnetic centers with $S = \frac{1}{2}$, $I = \frac{1}{2}$, $\nu_{\text{mw}} = 9.0$ GHz, $g_k = 2.0$, $\frac{1}{2\pi} a^k_{\text{iso}} = 500$ MHz, and $g_l = 2.1$, $\frac{1}{2\pi} a^l_{\text{iso}} = 350$ MHz. (a) EPR spectra of the single components. (b) EPR spectrum of both components. (c) Spin–echo oscillations caused by incrementing the modulation field amplitude ΔB_0. (d) 2D representation of the EZ-EPR spectrum with separated spectra of the two compounds along the g-value dimension.

echo sequence with the electron coherence evolving under the magnetic field

$$B_0(t) = B_0 + \Delta B_0 \sin\left(\frac{\pi t}{\tau}\right), \qquad [4]$$

where τ denotes the pulse spacing in the echo sequence (Fig. 2a). Thus, the first free evolution time has the length of the first half of a period of the sine modulation, and the second free evolution time has the length of the second half of a period of the sine modulation.

We now give an analytical description of the experiment and derive a formula for the accumulated phase of the electron coherence by applying the density operator formalism to two spin systems k and l with $S = \frac{1}{2}$ and g values $g_k \neq g_l$. Nonselective pulses and an inhomogeneously broadened EPR line are assumed. A visualization of the motion of the transverse magnetization in the rotating frame for the times indicated in Fig. 2a is given in Fig. 2b.

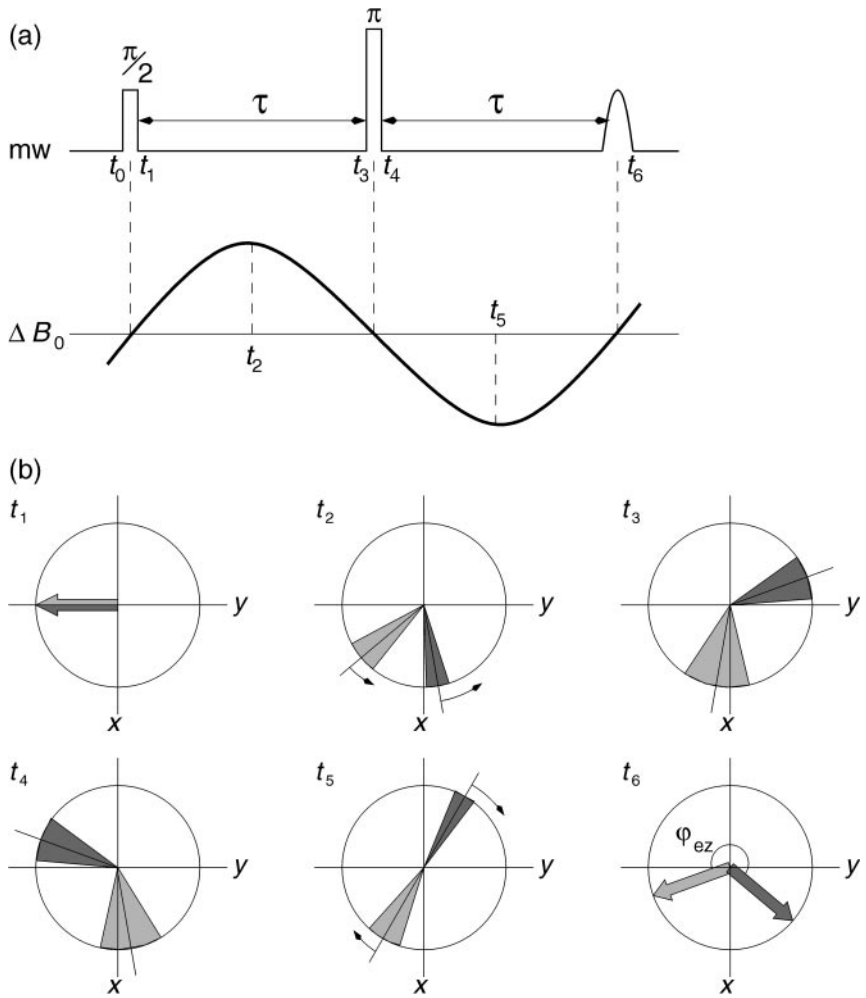

FIG. 2. Primary echo based EZ-EPR of an $S = \frac{1}{2}$ system. (a) Pulse sequence with a sinusoidal magnetic field modulation. (b) Visualization of the motion of the transverse magnetization in the rotating frame for two different species k and l with different g values, corresponding to the points in time indicated in (a). Tight gray areas: species k; dark gray areas: species l.

At Boltzmann equilibrium, the magnetization is oriented along $\boldsymbol{B_0}$

$$\sigma_{t=t_0} = -S_z. \qquad [5]$$

The $\frac{\pi}{2}$ pulse along the x-axis rotates the longitudinal magnetization into the transverse plane and creates electron coherence

$$\sigma_{t=t_1} = S_y. \qquad [6]$$

During the following free evolution period the spin packets dephase because of the inhomogeneity of the EPR line. In addition, due to the magnetic field modulation, the spins precess in the xy-plane with their g-value specific Larmor frequency. Between the times t_1 and t_2 the modulation amplitude ΔB_0 increases so that the precession is accelerated, whereas between t_2 and t_3 the amplitude ΔB_0 decreases and the precessing spins are retarded. During this process, magnetization vectors with different g values accumulate different phase angles. During the evolution period the time-dependent Hamiltonian depends only on S_z. Thus, for any times $t_i \neq t_j$ the terms in the Hamiltonian commute, so that during the free evolution period the time-dependent Hamiltonian can be replaced by a time-independent Hamiltonian, with an integral frequency offset $\Omega_s + \bar{\Omega}_{\mathrm{ez}}$

$$\bar{\mathcal{H}}_0^{(+)} = (\Omega_s + \bar{\Omega}_{\mathrm{ez}})S_z, \qquad [7]$$

where the frequency offset is split into a time-independent part Ω_s which depends on B_0 and a time-dependent part, $\bar{\Omega}_{\mathrm{ez}}$, which depends on $\Delta B_0(t)$. With the formula

$$\varphi_{\mathrm{ez}}(\Delta B_0(t)) = \frac{g\,\beta_{\mathrm{e}}}{\hbar}\Delta B_0 \int_0^{\tau} \mathrm{d}t\ f(t) \qquad [8]$$

the integral EZ offset $\bar{\Omega}_{ez}$ can be calculated to

$$\bar{\Omega}_{ez} = \frac{\varphi_{ez}}{\tau} = \frac{4g\beta_e}{h}\Delta B_0. \quad [9]$$

Thus, the first free evolution period of time τ leads to the density operator

$$\sigma_{t=t_3} = S_y \cos[(\Omega_s + \bar{\Omega}_{ez})\tau] - S_x \sin[(\Omega_s + \bar{\Omega}_{ez})\tau]. \quad [10]$$

The refocusing π pulse along x inverts the magnetization

$$\sigma_{t=t_4} = -S_y \cos[(\Omega_s + \bar{\Omega}_{ez})\tau] - S_x \sin[(\Omega_s + \bar{\Omega}_{ez})\tau]. \quad [11]$$

During the second free evolution period of time τ the field modulation is opposite in sign which leads to the opposite EZ offset

$$\bar{\mathcal{H}}_0^{(-)} = (\Omega_s - \bar{\Omega}_{ez})S_z. \quad [12]$$

During refocusing again phase is accumulated. Finally, at time of echo formation we find

$$\sigma_{t=t_6} = -S_y \cos(2\bar{\Omega}_{ez}\tau) - S_x \sin(2\bar{\Omega}_{ez}\tau). \quad [13]$$

The frequency offsets Ω_s are thus refocused to a primary echo

$$s(t = t_6) = \exp(i\varphi_{ez}) \quad [14]$$

with the phase

$$\varphi_{ez} = 2\bar{\Omega}_{ez}\tau = \frac{8g\beta_e}{h}\Delta B_0\tau, \quad [15]$$

which is proportional to the field modulation amplitude ΔB_0 and the corresponding g value. The variable phases of these g-value specific spin echoes in the xy-plane cause the component of the net spin echo along the y-axis to oscillate as a function of the modulation amplitude ΔB_0 (Fig. 1c).

3. NUMERICAL SIMULATIONS OF TWO-DIMENSIONAL EZ-EPR SPECTRA

EZ-EPR spectra manifest in a very different way compared to conventional EPR spectra, which particularly holds for spectra of disordered systems. To become more familiar with the appearance of 2D EZ-EPR spectra of polycrystalline samples, a number of numerical computations will be presented.

Figure 3 shows different situations for anisotropic $S = \frac{1}{2}$ spin systems at X-band ($\nu_{mw} = 9$ GHz). In these plots the horizontal axis represents the B_0 field, and the vertical axis represents the g-value dimension. Figure 3a shows an EZ-EPR spectrum without hyperfine interaction. The spectrum consists of a single ridge, extended from the minimum resonance field $B_\parallel$ to the maximum field $B_\perp$, and from the maximum g value $g_\parallel = 2.2$ to the minimum g value $g_\perp = 2.0$. Figure 3b illustrates the effect of an *isotropic* hyperfine coupling of an $I = \frac{1}{2}$ nucleus with $\frac{1}{2\pi}a_{iso} = 100$ MHz on the EZ-EPR spectrum. A ridge for each of the two values of the nuclear magnetic quantum number m_I is observed. A slice at any fixed g value results in an EPR spectrum with two peaks split by $\frac{a_{iso}}{g\beta_e}$. In Fig. 3c, the hyperfine tensor is assumed to be *anisotropic*, with principal values $\frac{1}{2\pi}A_\parallel = 500$ MHz and $\frac{1}{2\pi}A_\perp = 100$ MHz, and coaxial with the g tensor. In Fig. 3d, an additional hyperfine coupling of an $I = 1$ nucleus with $\frac{1}{2\pi}a_{iso} = 40$ MHz is introduced, resulting in a splitting of the two ridges into triplets. Slices for fixed g values facilitate the monitoring of such a hyperfine structure at any orientation, which is not possible in conventional field-swept EPR, where the hyperfine structure can only be observed at canonical orientations. In Fig. 3e, the EZ-EPR spectrum of a spin system with $I = \frac{1}{2}$, orthorhombic symmetry and coaxial g and hyperfine tensors is depicted, with principal values $g_x = 2.00$, $g_y = 2.05$, $g_z = 2.20$, $\frac{1}{2\pi}A_x = 500$ MHz, $\frac{1}{2\pi}A_y = 50$ MHz, and $\frac{1}{2\pi}A_z = 200$ MHz. A pronounced increase in resolution is achieved for a slice at g_y, providing the pure A_y hyperfine structure together with hyperfine couplings of other orientations. Finally, in Fig. 3f, the axial g and hyperfine tensors are assumed to be noncoaxial with an angle $\delta = 60^\circ$ between $g_\parallel$ and $A_\parallel$. Slices for a fixed g value show cross sections of the ridges which are broadened due to the noncoaxiality. They are a measure for the distribution of the hyperfine couplings at a given orientation.

In all these spectra the sum projection of the EZ-EPR plot onto the B_0-field axis results in the conventional field-swept EPR spectra and onto the g-value axis in the corresponding g-value spectra, which are free of hyperfine splittings.

A model calculation for a polycrystalline sample with $S = \frac{1}{2}$ and a nucleus with $I = \frac{3}{2}$ is shown in Fig. 4, with parameters typical for a planar copper complex ($g_\parallel = 2.18$, $g_\perp = 2.02$, $\frac{1}{2\pi}A_\parallel = -600$ MHz, $\frac{1}{2\pi}A_\perp = -50$ MHz) and a microwave (mw) frequency of $\nu_{mw} = 9.1$ GHz. Because of the large g and A anisotropy, the EPR spectrum shown in Fig. 4a is difficult to interpret, in particular in the high-field region. In the corresponding EZ-EPR spectrum (Fig. 4b) one ridge for each value of m_I is observed. In this plot, the extra-absorption peak (*20*) of the $m_I = \frac{3}{2}$ ridge, which is often observed in spin systems with strongly anisotropic g and hyperfine tensors, becomes evident. It results from regions on the resonance surface where $\frac{dB_{res}}{d\theta} = 0$, which do not coincide with one of the canonical orientations of the g and hyperfine tensors.

For an axially symmetric spin system, a slice at a fixed g value represents the EPR spectrum of species for which the B_0-field

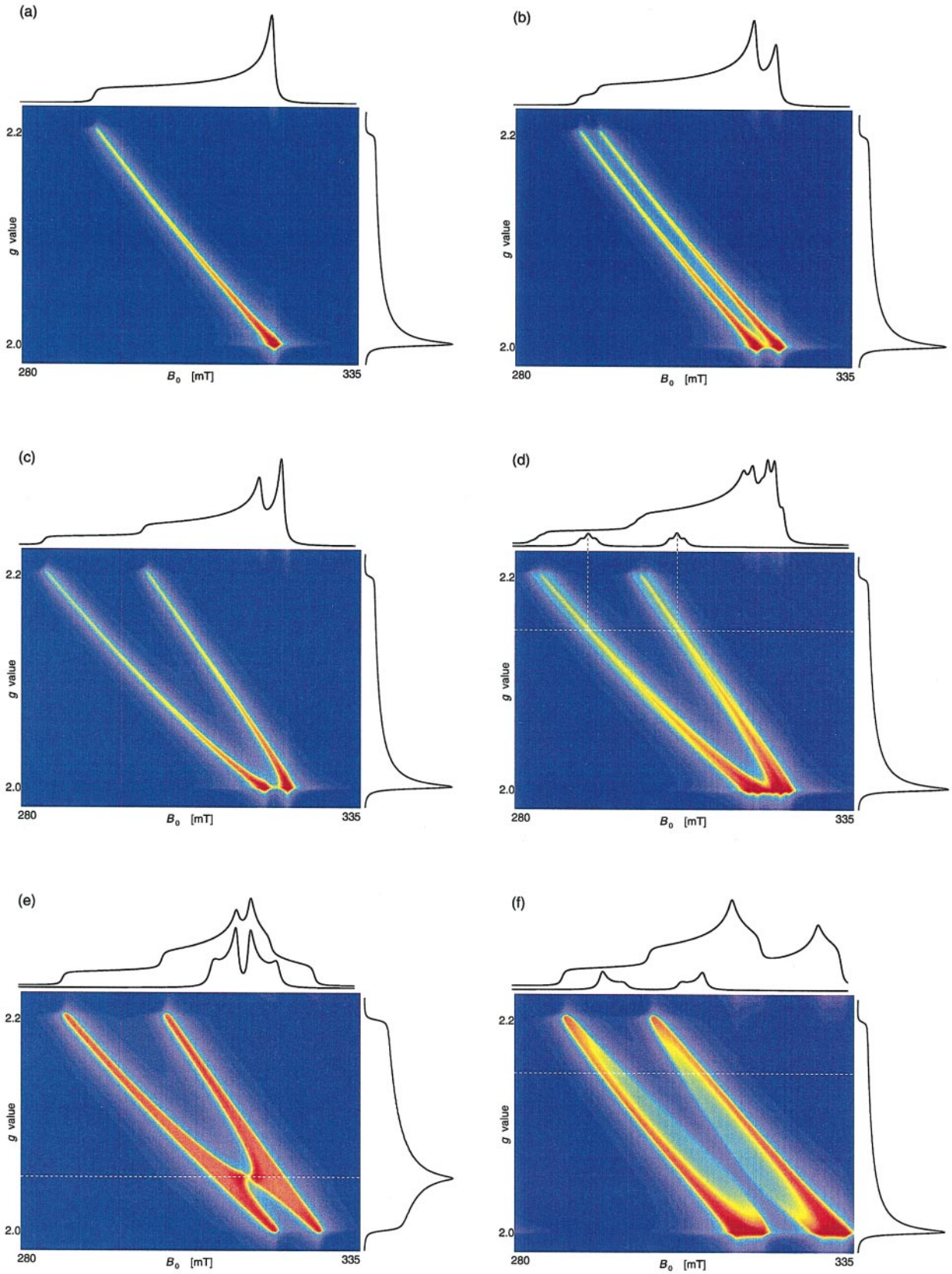

FIG. 3. Numerical simulations of 2D powder EZ-EPR spectra, together with the corresponding projections on the B_0-field and g-value axes. In (d–f) also a slice for g = const. is shown. (a) $S=\frac{1}{2}$, $I=0$ and an axial g tensor. (b) $S=\frac{1}{2}$, $I=\frac{1}{2}$, axial g tensor and isotropic hyperfine coupling. (c) $S=\frac{1}{2}$, $I=\frac{1}{2}$ and axial g and hyperfine tensors. (d) $S=\frac{1}{2}$, $I=\frac{1}{2}$, axial g and hyperfine tensors, and additional isotropic hyperfine coupling with $I=1$. (e) $S=\frac{1}{2}$, $I=\frac{1}{2}$, and orthorhombic g and hyperfine tensors. (f) $S=\frac{1}{2}$, $I=\frac{1}{2}$, and axial but noncoaxial g and hyperfine tensors.

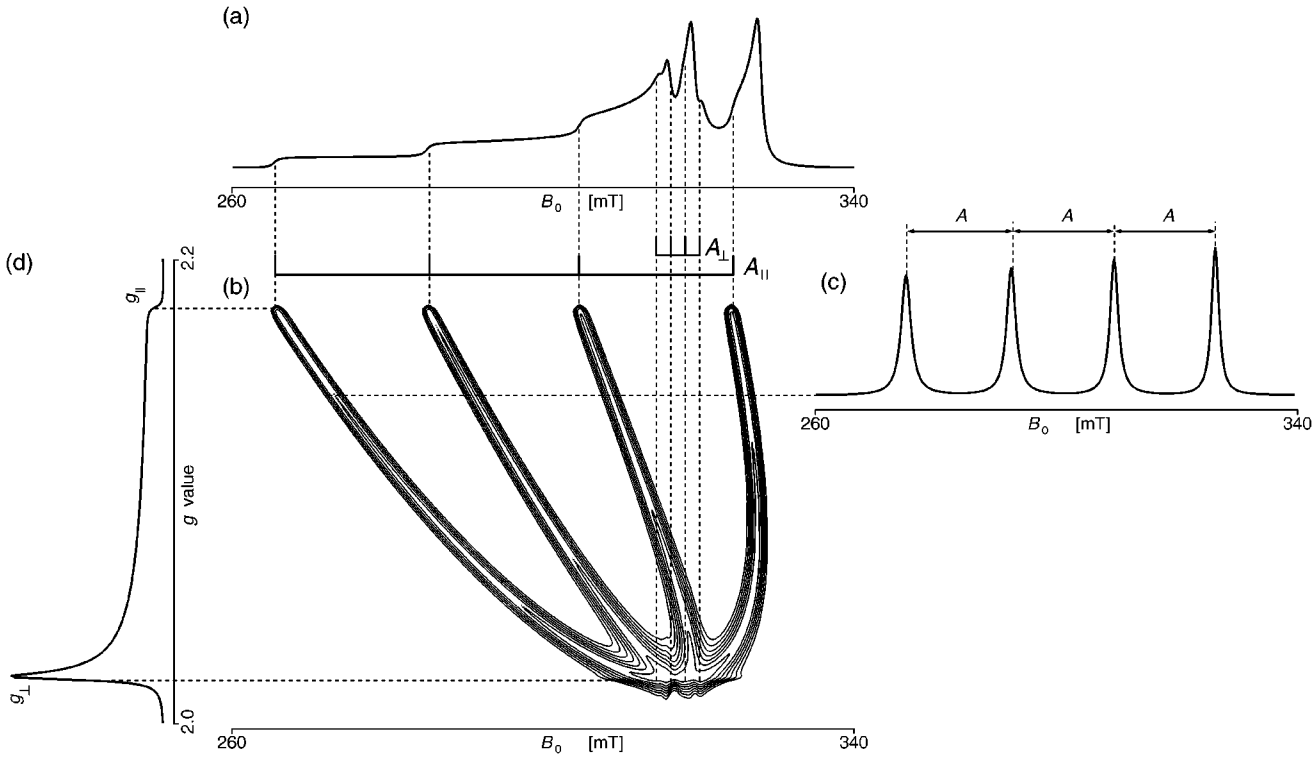

FIG. 4. Numerical simulation of a powder EZ-EPR spectrum typical for a copper complex. (a) Conventional EPR spectrum. (b) 2D EZ-EPR spectrum with stack plots for the hyperfine splitting and indicated principal values $g_\parallel$, $g_\perp$, $A_\parallel$, and $A_\perp$. (c) Slice at $g = 2.15$, corresponding to a polar angle $\theta = 26.1^\circ$ with indicated hyperfine splitting A. (d) g-value spectrum with indicated principal values $g_\parallel$ and $g_\perp$.

vectors lie on a cone with axis along $g_\parallel$ and an opening angle

$$\theta = \arcsin\left(\frac{g^2 - g_\parallel^2}{g_\perp^2 - g_\parallel^2}\right)^{1/2}. \qquad [16]$$

Thus, hyperfine couplings for such an angle can easily be determined from slices with $g = \text{const}$. As an example the spectrum for $g = 2.15$ corresponding to $\theta = 24^\circ$ and a hyperfine coupling of $\frac{1}{2\pi} A_{\theta=24^\circ} = -527$ MHz, is depicted in Fig. 4c.

The sum projection onto the g-value axis gives the g-value spectrum free of hyperfine interactions, as shown in Fig. 4d, which allows for an accurate determination of $g_\parallel$ and $g_\perp$.

4. EXPERIMENTAL

All experiments presented in this work were carried out on a home-built X-band pulse EPR spectrometer (*21*) with a home-built dielectric ring resonator (*14*) at a temperature of 15 K. A two-pulse sequence with pulse lengths of $t_p = 20$ ns, pulse spacings of $\tau = 980$ ns, and a field modulation of frequency $\nu_{ez} = 500$ kHz was applied. The supplementary equipment required for the EZ-EPR experiment will be described in detail elsewhere. The setup for the field modulation consists of an arbitrary function generator (AFG, LeCroy 9100), a radio frequency (rf) amplifier (AR 100A500A), and a Helmholtz coil for the field modulation. A schematic representation is given in Fig. 5.

The magnetic field modulation was generated with a Helmholtz coil placed around a dielectric ring resonator operating in the TE_{011} mode. The orientation of the field modulation should coincide with that of the static field within about $\pm 5^\circ$. The sine modulation was generated by the AFG with a computer controlled amplitude, triggered by the mw pulse sequence. To obtain sufficiently high modulation amplitudes an LC resonance circuit consisting of the Helmholtz modulation coil ($L = 165.8\ \mu$H) and a tunable capacitor (C variable from 8 pF to 1 nF) was used. The modulation amplitude was optimized by matching the impedance of the resonance circuit to the rf amplifier. The linearity of the rf amplifier is of major importance, in order to achieve small linewidths in the g-value dimension. The EZ sequence is programmed in a way that the center of the mw pulses occur at exact zero-crossings of the field modulation, whereas the position of the spin echo is delayed in time by $t_p/2$, which is due to the width of the EPR line being broader than the frequency range excited with the mw pulses (*22*).

With this setup, a maximum field strength at the sample position of $\Delta B_0 = 20$ mT was obtained. The measuring time varies between about 2 h for a single-crystal spectrum to approximately 12 h for a powder spectrum and strongly depends upon the complexity of the system concerning the desired g-value resolution and the signal-to-noise ratio.

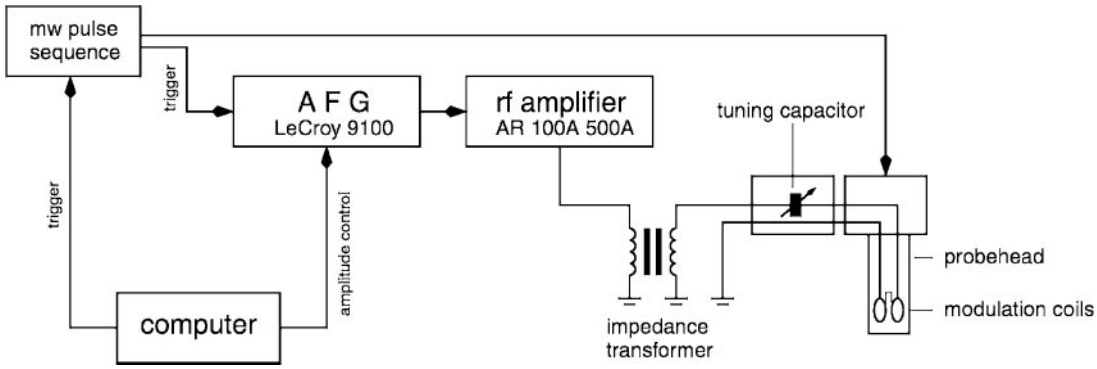

FIG. 5. Schematic representation of the additional setup for EZ-EPR experiments.

The attainable resolution in the g-value dimension is limited by different contributions.

(a) Excitation bandwidth: The fragment of the EPR spectrum, and as a consequence the range of g values, which is excited by the mw pulses, is determined by the width of the pulses. A short pulse leads to narrow lines in the g-value dimension, if the width of an EPR spectrum is mainly caused by hyperfine or fine-structure anisotropy. On the other hand, broad lines in the g-value spectrum are expected for pronounced g anisotropy.

An upper limit can be given for the linewidth in the g-value dimension, neglecting instrumental imperfections. The excitation bandwidth of a two-pulse echo sequence with pulses of length t_p is approximately $\frac{1}{2\,t_p}$ (*1*), so that the resolution for a system with pure g anisotropy is given by

$$\Delta g = \frac{2h}{\beta_e B_0 t_p}. \qquad [17]$$

For typical experimental values the upper limit for the resolution in the g-value dimension is on the order of $\Delta g \approx 10^{-2}$. For any other system, where for example hyperfine or fine structure interactions cause the anisotropy, this value is expected to be smaller.

(b) Instrumental imperfections: A prerequisite for small linewidths in the g-value dimension is a high spatial homogeneity of the modulation field over the sample volume. The dephasing of coherence due to an inhomogeneity of the modulation field is not refocused in this experiment, and thus causes a faster decay of the spin echo that results in a line broadening in the g-value dimension.

Furthermore, the field modulation may induce eddy currents in any metallic surface which in turn cause an additional field inhomogeneity. To reduce the eddy currents, closed metallic surfaces have been avoided in the vicinity of the sample and even in the cryostat.

In addition, imperfections of the modulation amplifier, such as nonlinearities and phase instabilities relative to the pulse sequence, may cause modulation effects on the spin echo resulting in a further broadening of the lines.

(c) Influence of finite pulse lengths: In real experiments the pulses and the echo are of finite length so that the modulation field changes during the mw pulses and the detection of the echo. Therefore we have to compromise between the pulse lengths and the finite times for zero crossings of $\Delta B_0(t)$. The change dB_0 of the modulation field during the application of an mw pulse of length t_p can be expressed as

$$dB_0 = 2\Delta B_0 \sin\left(\frac{\omega_{ez} t_p}{4\pi}\right). \qquad [18]$$

For $\frac{1}{2\pi}\omega_{ez} = 500$ kHz, and typical values of $t_p = 20$ ns and $\Delta B_0 = 10$ mT, the resulting change in modulation field is on the order of $dB_0 \approx 10^{-3}$ mT, which can be neglected. The same consideration holds for the influence of the field change on the echo formation.

5. RESULTS

To estimate the experimental limits and to demonstrate the potential of the method, several EZ-EPR experiments were carried out. The spectral analysis consisted of four steps (i) Baseline correction, (ii) Zero-filling to 256 data points, (iii) Apodization with a Gaussian window (if necessary), and (iv) Fourier tranformation with respect to ΔB_0.

Separation of the Overlapping Spectra of Two Sites in a Single Crystal

EZ-EPR can be used to disentangle overlapping single-crystal spectra originating from magnetically nonequivalent sites in a crystal lattice, provided the g values of the sites differ sufficiently from each other. This is demonstrated on a copper-doped glycine single crystal (*23, 24*) with spectra of the two sites that overlap for all orientations. Each spectrum consists of four copper transitions split into a quintet due to the hyperfine interaction with two magnetically equivalent nitrogen nuclei. The echo-detected X-band EPR spectrum for an arbitrary crystal orientation is shown in Fig. 6a. In the EZ-EPR contour plot in Fig. 6b, the spectra of

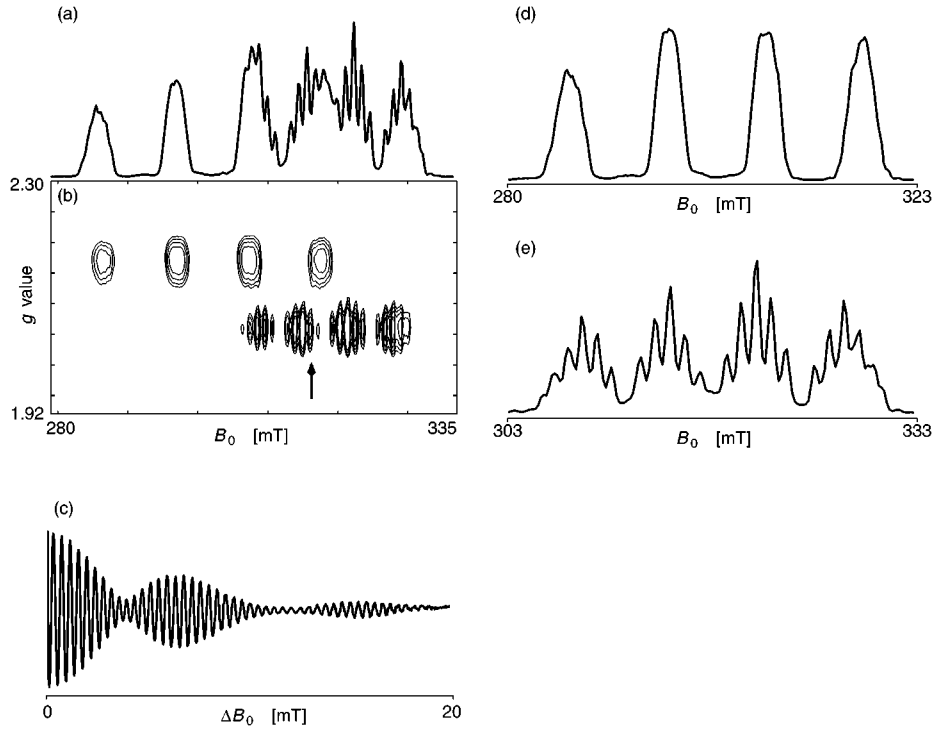

FIG. 6. EPR spectra of a copper-doped glycine single crystal, $Cu(gly)_2$; mw frequency $\nu_{mw} = 9.15$ GHz, temperature $T = 15$ K; measuring time ≈ 2 h. (a) Two-pulse echo-detected EPR spectrum; pulse lengths $t_{\pi/2} = t_\pi = 20$ ns, interpulse delay $\tau = 980$ ns. (b) 2D EZ-EPR spectrum. (c) Echo-oscillation trace recorded at $B_0 = 318$ mT (arrow in (b)). (d, e) Slices at the g values of the two sites.

the two sites are fully separated. In this experiment, the modulation amplitude ΔB_0 was varied from 0 to 20 mT in steps of 0.25 mT.

Figure 6c shows an echo oscillation trace as a function of ΔB_0, recorded at $B_0 = 318$ mT (arrow in Fig. 6b). Slices representing the spectra of the two sites (site 1 at $g_1 = 2.17$, site 2 at $g_2 = 2.06$) are depicted in Figs. 6d and 6e.

EZ-EPR Experiment on a Polycrystalline Sample

Copper complexes often show a nearly axial g tensor with a coaxial hyperfine coupling of the copper nucleus. It is usually straightforward to determine from a polycrystalline sample the parallel values $g_\parallel$ and $A_\parallel$; the determination of the corresponding perpendicular values $g_\perp$ and $A_\perp$ is much more difficult. Moreover, in a conventional field-swept EPR spectrum only the principal values are accessible, because a superposition of the spectra of all orientations between the principal directions manifests in broad features without any structure. This is in contrast to the corresponding 2D EZ-EPR spectrum where g and hyperfine values for all orientations can be measured. Beyond that it is possible to identify extra-absorption peaks. We illustrate this on bis(salicylaldoximato)^{63}Cu(II), $^{63}Cu(sal)_2$, diluted into $Ni(sal)_2$ powder (*25, 26*). In this complex hyperfine interactions with the $I^{Cu} = \frac{3}{2}$ copper nucleus and two magnetically equivalent $I^N = 1$ nitrogen nuclei can be observed. The relatively large g anisotropy causes a fast decay of the spin–echo oscillation. Therefore the influence of instrumental imperfections on the linewidth are only moderate.

In Fig. 7a the two-pulse echo-detected, powder EPR spectrum, recorded at an mw frequency of $\nu_{mw} = 9.095$ GHz, is depicted. The high-field region of the spectrum is characterized by an overlap of many spectral components with g values between $g_\parallel$ and $g_\perp$, and hyperfine splittings due to copper and nitrogen couplings. Because of these overlapping features, an unambiguous determination of the magnetic parameters is not possible in this field region, without extensive spectral simulations.

The 2D EZ-EPR spectrum was recorded by varying the modulation amplitude from 0 to 15 mT in steps of 0.2 mT. A contour plot of the 2D EZ-EPR spectrum is shown in Fig. 7b. The four ridges indicating the four m_I states of the copper nucleus are clearly visible. The obtained parameters of the spin Hamiltonian listed in Table 1, agree quite well with data found in literature. It was also possible to identify the extra-absorption peak of the $m_I = \frac{3}{2}$ manifold, at which the resonance field is larger than $B_\parallel$ and $B_\perp$. The hyperfine coupling of the copper nucleus at arbitrary orientations could also be determined. A cross section at $g = 2.1$ is shown in Fig. 7c. In this spectrum, the peak for the $m_I = \frac{3}{2}$ manifold is best resolved, because the slice is taken along an axis perpendicular to the corresponding ridge in the 2D EZ-EPR spectrum. It reveals a structure corresponding to the expected number of the nitrogen splittings (theoretical

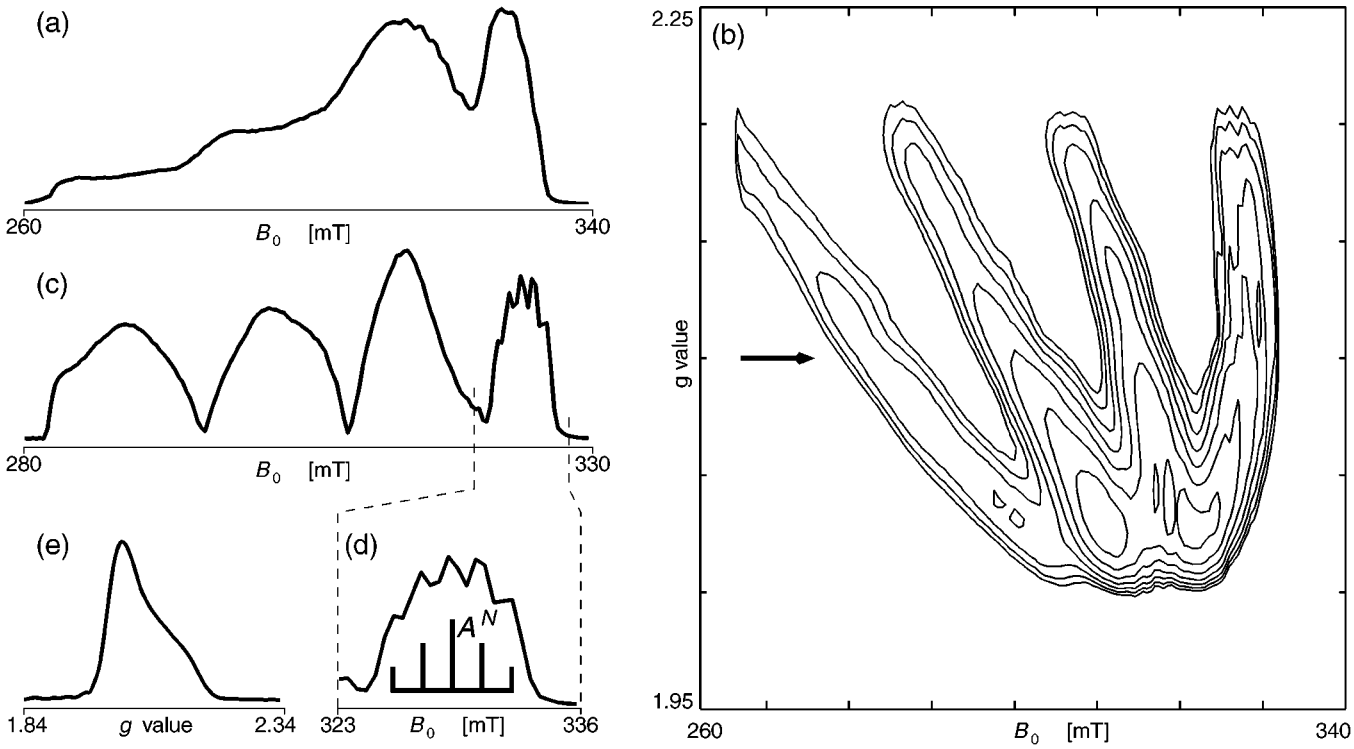

FIG. 7. EPR spectra of bis(salicylaldoximato)^{63}Cu(II), ^{63}Cu(sal)$_2$; mw frequency $\nu_{mw} = 9.15$ GHz, temperature $T = 15$ K; measuring time ≈ 6 h. (a) Two-pulse echo-detected EPR spectrum; pulse lengths $t_{\pi/2} = t_\pi = 20$ ns, interpulse delay $\tau = 980$ ns. (b) 2D EZ-EPR spectrum. (c) Slice for $g = 2.1$ (arrow in (b)). (d) Enlarged section of the $m_I = \frac{3}{2}$ manifold with stack plot for the expected nitrogen hyperfine splitting. (e) g-value spectrum.

intensities 1 : 2 : 3 : 2 : 1), indicating that two nitrogen nuclei are involved (Fig. 7d). This information cannot easily be obtained from other methods, such as ENDOR. The nitrogen hyperfine coupling was found to be $\frac{1}{2\pi}A^N = 46$ MHz (Table 1), in good agreement with values known from the literature. The enhanced resolution in slices with fixed g values is due to the orientation selection mentioned in Section 3; only orientations on a cone with fixed opening angle are monitored, rather than a superposition of orientations with a wide range of angles θ characteristic for a polycrystalline sample.

The sum projection along the second dimension of the 2D EZ-EPR spectrum, shown in Fig. 7e, gives the g-value spectrum. The characteristic shape for an axially symmetric g tensor is clearly visible, and the $g_\parallel$ and $g_\perp$ principal values can easily be extracted from this spectrum.

TABLE 1
Measured g Values and Hyperfine Couplings (in MHz) for ^{63}Cu(sal)$_2$

Method/system	$g_\parallel$	$g_\perp$	$A_\parallel^{Cu}$	$A_\perp^{Cu}$	$A_\perp^{N}$	
EZ-EPR (^{63}Cu) Cu(sal)$_2$ in Ni(sal)$_2$ powder	2.20	2.03	−600	−120	46	this work
Frozen-solution EPR Cu(sal)$_2$ in 40% toluene 60% chloroform	2.171	2.020	−610	−137	47	(*25*)
Single-crystal EPR Cu(sal)$_2$ in Ni(sal)$_2$	2.203	2.048	−609	−110	46	(*26*)

Separation of Two Powder Spectra

Analogous to the separation of overlapping spectra of different sites in single crystals, EZ-EPR also allows the separation of overlapping powder spectra of compounds with ranges of g values that do not overlap. As an example, the spectrum of bis(acetylacetonato)Cu(II), Cu(acac)$_2$, with $g_\perp = 2.053 \le g \le g_\parallel = 2.266$ (*27*) and of VO(acac)$_2$ with $g_\parallel = 1.95 \le g \le g_\perp = 1.98$, both diluted into Pd(acac)$_2$ powder,

TABLE 2
Measured g Values and Hyperfine Couplings (in MHz) for Cu(acac)$_2$

Method/system	$g_\parallel$	$g_\perp$	$A_\parallel^{Cu}$	$A_\perp^{Cu}$	
EZ-EPR Cu(acac)$_2$ in Pd(acac)$_2$ powder	2.27	2.05	−558	−65	this work
Single-crystal EPR Cu(acac)$_2$ in Pd(acac)$_2$	2.266	2.053	−534	−63	(*27*)
Powder EPR Cu(acac)$_2$ in Pd(acac)$_2$	2.264	2.052	−607	−69	(*28*)

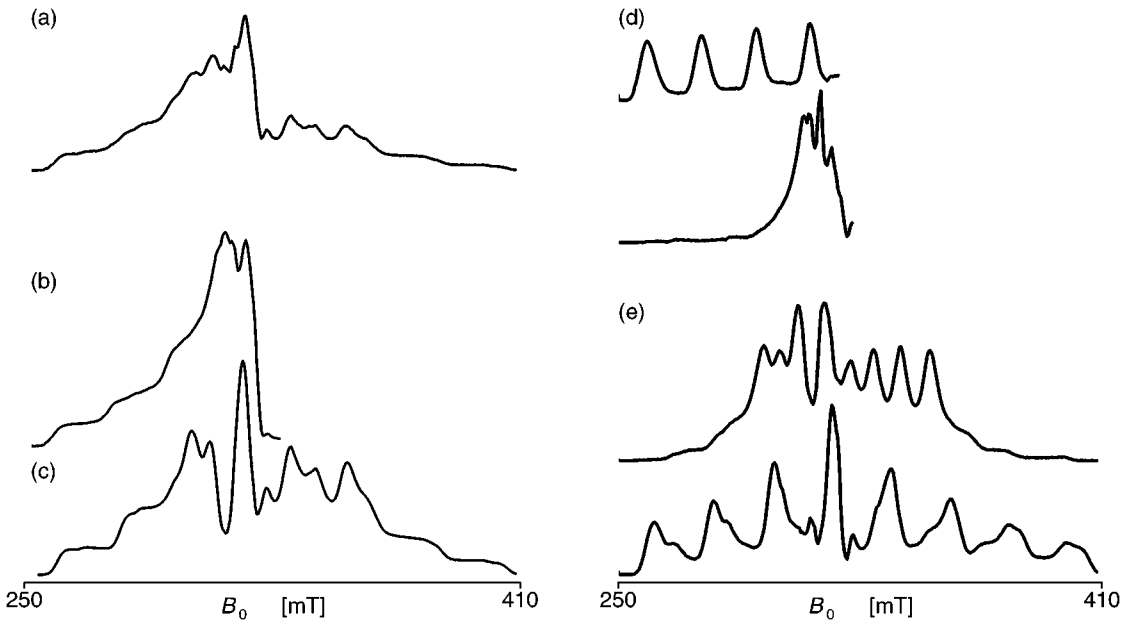

FIG. 8. EPR spectra of a sample consisting of bis(acetylacetonato)Cu(II), $Cu(acac)_2$, and $VO(acac)_2$ in $Pd(acac)_2$ powder; mw frequency $\nu_{mw} = 9.15$ GHz, temperature $T = 15$ K; measuring time ≈ 12 h. (a) Two-pulse echo-detected EPR spectrum; pulse lengths $t_{\pi/2} = t_\pi = 20$ ns, interpulse delay $\tau = 980$ ns. (b, c) Projected 1D EZ-EPR spectra of $Cu(acac)_2$ (b) and $VO(acac)_2$ (c). (d) Slices at $g_\parallel$ (top) and $g_\perp$ (bottom) of the EZ-EPR spectrum for $Cu(acac)_2$. (e) Slices at $g_\perp$ (top) and $g_\parallel$ (bottom) of the EZ-EPR spectrum for $VO(acac)_2$.

are separated. The EPR spectra of the two species fully overlap in the field dimension because of hyperfine splitting, as shown in Fig. 8a, and an unambiguous interpretation of the observed spectrum is not possible.

For the EZ-EPR experiment, the modulation amplitude ΔB_0 was varied from 0 to 15 mT in steps of 0.1 mT. The gap of $\Delta g = 0.07$ between the g values $g_\perp^{V}$ and $g_\perp^{Cu}$ is sufficient for a full separation of the two individual spectra (Fig. 9). The ridges of the $VO(acac)_2$ complex are not as well resolved as the ridges of $Cu(acac)_2$. This is mainly due to different g anisotropies of the two paramagnetic species. Whereas for $Cu(acac)_2$ the anisotropy is $\Delta g = 0.213$, it is only $\Delta g = 0.03$ for $VO(acac)_2$.

Projections of the individual EZ-EPR spectra onto the B_0-field axis yield the individual spectra of the two species (Figs. 8b and 8c). The projected spectra are almost identical with spectra recorded with samples containing only one of the components.

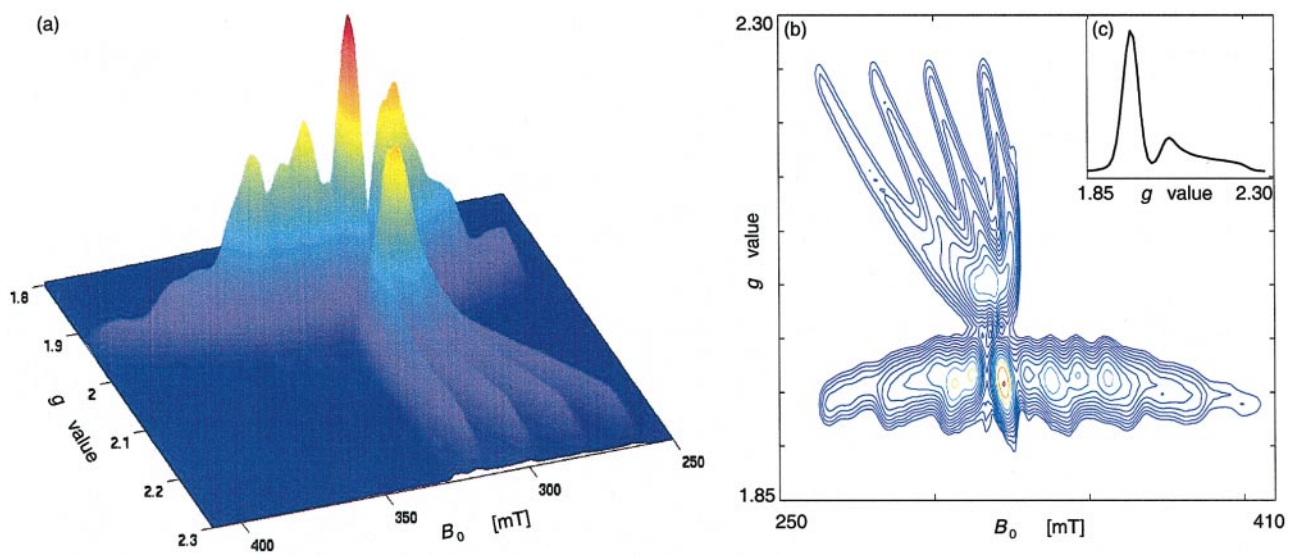

FIG. 9. EZ-EPR spectra of a sample consisting of bis(acetylacetonato)Cu(II), $Cu(acac)_2$, and $VO(acac)_2$ in $Pd(acac)_2$ powder; parameters as in Fig. 8. (a) Surface plot. (b) Contour plot. (c) g-value spectrum.

TABLE 3
Measured g Values and Hyperfine Couplings (in MHz) for $VO(acac)_2$

Method/system	$g_\parallel$	$g_\perp$	$A_\parallel^V$	$A_\perp^V$	
EZ-EPR $VO(acac)_2$ in $Pd(acac)_2$ powder	1.95	1.98	536	216	this work
Frozen-solution EPR $VO(acac)_2$ in THF	1.945	1.980	560	210	(*29*)
Liquid-crystal EPR $VO(acac)_2$ in nematic liquid crystal	1.945	1.979	560	207	(*30*)

Slices for the canonical orientations $g_\parallel$ and $g_\perp$ are depicted in Fig. 8d for $Cu(acac)_2$ and in Fig. 8e for $VO(acac)_2$, respectively. The obtained values of the spin–Hamiltonian parameters are summarized in Tables 2 and 3. The signs of the hyperfine couplings were taken from the literature. For $A_\perp^{Cu}$ of $Cu(acac)_2$ the relatively large second-order shifts in the hyperfine splittings can be nicely seen, which shift the resonance lines to higher fields and results in a monotonic increase in the spacing of the hyperfine splitting with increasing B_0 field; these second-order effects being in the order of 15–30 MHz at X-band frequencies (*28*). The difference in the hyperfine splittings is further increased by the nuclear quadrupole interaction; the quadrupole effects being comparable in magnitude to the effects arising from the second-order hyperfine interaction. The two types of second-order correction add for the hyperfine splitting at the high-field end of the EPR spectrum, and tend to cancel for the hyperfine splitting at the low-field end. Therefore the best value for the hyperfine coupling is obtained by considering only the low-field hyperfine splitting.

In this example, a B_0-field of more than 1 T would be required in a conventional EPR experiment for a full separation of the two spectra. Even though in cases where the g-value ranges of two or more spectra overlap, EZ-EPR spectroscopy may still be useful, since for wide g-value ranges of one of the components there is usually still no overlap with features of the second species.

6. CONCLUSION AND OUTLOOK

In this work we demonstrated that EZ-EPR allows the disentangling of EPR spectra into a second, g-value dependent dimension. With EZ-EPR overlapping features of polycrystalline EPR spectra can be separated and extra absorption peaks can be identified. Moreover, the method enables us to determine hyperfine couplings at orientations that differ from the canonical orientations, and projections of EZ-EPR spectra onto the new dimension yield pure g-value spectra. This allows the determination of the principal values of the g tensors even in cases where the evaluation of these parameters is made difficult or impossible due to extensive hyperfine couplings or zero-field splittings.

Furthermore, overlapping powder EPR spectra of compounds with different g-value ranges and single-crystal EPR spectra with magnetically nonequivalent sites can be separated. EZ-EPR may therefore be regarded in some respects as an alternative to high-field EPR spectroscopy. To separate overlapping EPR spectra of compounds with different g values EZ-EPR may even go beyond the possibilities of high-field EPR, because spectra that overlap in the B_0-field dimension are separated due to an expansion into a *new*, g-value dependent dimension, rather than due to shifts of the spectra along the B_0-field axis.

With our current experimental setup, the attainable resolution in the g-value dimension is $\Delta g \approx 10^{-2}$. Hence, this resolution is not yet sufficient for EZ-EPR spectroscopy to become applicable to investigate radicals in frozen solutions with anisotropies typically of about $\Delta g \approx 0.005$.[2] An EZ-EPR scheme is under development which allows the separation of *two* overlapped spectra in single crystals or liquid solutions with g values that differ only by $\Delta g \approx 10^{-3}$ or less.

EZ-EPR is of great generality, as it is applicable to any paramagnetic system with an anisotropic electron-Zeeman interaction. The main advantage of this new EZ-EPR approach compared to previous developments is that the mw pulses and the spin echo are set at $\Delta B_0(t) = 0$, i.e., at on-resonance conditions, independent on the modulation amplitude ΔB_0. Furthermore, the modulated spin–echo amplitude is acquired with constant evolution time τ. The measurement of the g-value spectrum is therefore free of relaxational decays.

The method works best for systems with large anisotropy. The less the anisotropy, the longer the modulation in the ΔB_0 dimension lasts. Because of the experimentally limited amplitude of ΔB_0^{max} the length of the modulation trace is also limited, which may lead to truncation effects of the echo oscillation trace. Since relatively long τ values have to be used and the phase memory time T_m of the electron spins is usually short, the echo amplitude in primary echo based EZ-EPR is often small. Hence samples with long T_m are advantageous. A stimulated echo based approach for EZ-EPR is under development to circumvent this loss in sensitivity. Furthermore, EZ-ESEEM experiments with a nuclear-frequency dimension and a g-value dimension become feasible, in order to improve the spectral resolution in ESEEM spectra. Because EZ-EPR can also be performed with commercially available components, the implementation of the experiment is quite straightforward and there is no need to build a dedicated probehead or a specialized spectrometer.

ACKNOWLEDGMENTS

This research has been supported by the Swiss National Science Foundation. The authors thank Gustavo Sierra who made the first steps in the development of this method, Jörg Forrer for general technical assistance, and Walter Lämmler for the preparation of the samples.

[2] For example, for the Y_D tyrosyl radical in photosystem II the g values are found to be $g_x = 2.00782$, $g_y = 2.00450$, $g_z = 2.00232$ (*31*), and for the nitroxide radical TEMPONE they are $g_x = 2.0104$, $g_y = 2.0074$, $g_z = 2.0026$ (*32*).

REFERENCES

1. A. Schweiger and G. Jeschke, "Principles of Pulse Electron Paramagnetic Resonance," Oxford Univ. Press, Oxford (2001).
2. J. R. Pilbrow, "Transition Ion Electron Paramagnetic Resonance," Clarendon, Oxford (1990).
3. L. O. Anderson and L. Clarkson, Field modulation phase detection techniques, *EPR Lett.* **1,** 4–5 (1980). [Varian]
4. M. Mehring, H. Seidel, W. Müller, and G. Wegner, Time resolved ESR of paramagnetic defects in undoped polyacetylene, *Solid State Commun.* **45,** 1075–1077 (1983).
5. E. Hoffmann and A. Schweiger, Inversion-recovery detected EPR, *Appl. Magn. Reson.* **9,** 1–22 (1995).
6. M. Willer and A. Schweiger, Forbidden-transition-labeled EPR (FORTE)—An approach for the sensitive measurement of forbidden EPR transitions, *Chem. Phys. Lett.* **230,** 67–74 (1994).
7. A. Schweiger, Orientation-modulated ESR spectroscopy, *J. Magn. Reson.* **51,** 286–300 (1983).
8. G. A. Sierra and A. Schweiger, Anisotropy-resolved electron paramagnetic resonance spectroscopy, *Mol. Phys.* **95,** 973–987 (1998).
9. A. V. Astashkin and A. Schweiger, Electron-spin transient nutation—A new approach to simplify the interpretation of ESR spectra, *Chem. Phys. Lett.* **174,** 595–602 (1990).
10. S. Stoll, G. Jeschke, M. Willer, and A. Schweiger, Nutation-frequency correlated EPR spectroscopy: The PEANUT experiment, *J. Magn. Reson.* **130,** 86–96 (1998).
11. Y. S. Lebedev, High-frequency continuous-wave electron spin resonance, *in* "Modern Pulsed and Continuous-Wave Electron Spin Resonance" (L. Kevan and M. K. Bowman, Eds.), Wiley, New York (1990).
12. L. C. Brunel, A. L. Barra, and G. Martinez, High-field electron-spin-resonance, *Physica B* **204,** 298–302 (1995).
13. G. A. Sierra, A. Schweiger, and R. R. Ernst, Electron-Zeeman resolved EPR, *Chem. Phys. Lett.* **184,** 363–367 (1991).
14. G. A. Sierra, Ph.D. thesis No. 1224 ETZ Zürich (1997).
15. R.-A. Eichel, G. A. Sierra, and A. Schweiger, Electron-Zeeman resolved EPR spectroscopy, *in* "Proceedings of the XXX Congress AMPERE on Magnetic Resonance, Lisbon" (2000).
16. M. Willer, J. Granwehr, J. Forrer, and A. Schweiger, Two-dimensional nuclear-Zeeman-resolved electron spin echo envelope modulation (NZ-ESEEM) spectroscopy, *J. Magn. Reson.* **133,** 46–52 (1998).
17. G. J. Bowden, J. M. Cadogan, J. Khachan, and R. P. Starrett, Elimination of T_2 decay problems in Zeeman-perturbed NQR experiments, *J. Magn. Reson.* **93,** 603–608 (1991).
18. G. J. Bowden, J. M., Pope, and F. Separovic, Zeeman-incremented multiple-quantum NMR, *J. Magn. Reson.* **103,** 307–312 (1993).
19. R. Wannemacher, D. Boye, Y. P. Wang, R. Pradham, W. Grill, J. E. Rives, and R. S. Meltzer, Zeeman-switched optical-free-induction decay and dephasing in $YLIF_4$-ER^{3+}, *Phys. Rev. B* **40,** 4237–4242 (1989).
20. V. Ovchinnikov and V. N. Konstantinov, Extra-absorption peaks in EPR spectra of systems with anisotropic g-tensor and hyperfine structure in powders and glasses, *J. Magn. Reson.* **32,** 179–190 (1978).
21. T. Wacker, Ph.D. thesis, No. 9913 ETH Zürich (1992).
22. W. B. Mims, Electron echo methods in spin resonance spectrometry, *Rev. Sci. Instrum.* **36,** 1472–1479 (1965).
23. M. Fujimoto, C. A. McDowell, and T. Takui, Ligand ENDOR spectra of Cu(II) impurity complexes in α-glycine crystals, *J. Chem. Phys.* **70,** 3694–3701 (1979).
24. C. A. McDowell, A. Naito, D. L. Sastry, Y. Cui, and K. Sha, Ligand ENDOR study of Cu(II)-doped α-glycylglycine single crystals at 4.2 K, *J. Phys. Chem.* **94,** 8113–8118 (1990).
25. H. R. Gersmann and J. D. Swalen, EPR spectra of copper complexes, *J. Chem. Phys.* **36,** 3221–3233 (1962).
26. A. Schweiger and H. H. Günthard, Single-crystal ESR and ENDOR of bis-(salicylaldoximato)Cu(II):bis-(salicylaldoximato)Ni(II): Copper, nitrogen and proton hyperfine data and structure of the internal H-bond, *Chem. Phys.* **32,** 35–61 (1978).
27. A. H. Maki and B. R. McGarvey, ESR in transition metal chelates. I. Copper(II) bis-acetylacetonate, *J. Chem. Phys.* **29,** 31–34 (1958).
28. L. D. Rollmann and S. I. Chan, Quadrupole effects in EPR spectra of polycrystalline copper and cobalt complexes, *J. Chem. Phys.* **50,** 3416–3431 (1969).
29. D. Kivelson and S. K. Lee, ESR studies and the electronic structure of Vanadyl ion complexes, *J. Chem. Phys.* **41,** 1896–1903 (1964).
30. B. Kirste and H. van Willigen, ENDOR study of bis(acetylacetonato)oxovanadium(IV) in frozen liquid crystals, *Chem. Phys. Lett.* **87,** 589–593 (1982).
31. C. T. Farrar, G. J. Gerfen, R. G. Griffin, D. A. Force, and R. D. Britt, Electronic structure of the Y-D tyrosyl radical in photosystem II: A high-frequency electron paramagnetic resonance spectroscopic and density functional theoretical study, *J. Phys. Chem.* **101,** 6634–6641 (1997).
32. O. H. Griffith, D. W. Cornell, and H. M. McConnell, Nitrogen hyperfine tensor and g tensor of nitroxide radicals, *J. Chem. Phys.* **43,** 2909–2910 (1965).